Available online at www.sciencedirect.com
ScienceDirect
Journal of Power Sources 160 (2006) 1009–1016
JOURNAL OF POWER SOURCES
www.elsevier.com/locate/jpowsour

Promising alloys for intermediate-temperature solid oxide fuel cell interconnect application

Shujiang Geng, Jiahong Zhu *

Department of Mechanical Engineering, Box 5014, Tennessee Technological University, Cookeville, TN 38505, USA

Received 7 December 2005; received in revised form 8 February 2006; accepted 9 February 2006
Available online 29 March 2006

Abstract

The formation of a low Cr-volatility and electrically conductive oxide outer layer atop an inner chromia layer via thermal oxidation is highly desirable for preventing chromium evaporation from solid oxide fuel cell (SOFC) metallic interconnects at the SOFC operation temperatures. In this paper, a number of ferritic Fe–22Cr alloys with different levels of Mn and Ti as well as a Ni-based alloy Haynes 242 were cyclically oxidized in air at 800 °C for twenty 100-h cycles. No oxide scale spallation was observed during thermal cycling for any of these alloys. A mixed Mn_2O_3/TiO_2 surface layer and/or a $(Mn, Cr)_3O_4$ spinel outer layer atop a Cr_2O_3 inner layer was formed for the Fe–22Cr series alloys, while an NiO outer layer with a Cr_2O_3 inner layer was developed for Haynes 242 after cyclic oxidation. For the Fe–22Cr series alloys, the effects of Mn and Ti contents as well as alloy purity on the oxidation resistance and scale area specific resistance were evaluated. The performance of the ferritic alloys was compared with that of Haynes 242. The mismatch in thermal expansion coefficient between the different layers in the oxide scale was identified as a potential concern for these otherwise promising alloys.

Keywords: Cyclic oxidation; Metallic interconnect; Solid oxide fuel cell; Spinel; Chromium evaporation; Area specific resistance

1. Introduction

One of the recent significant advancements in solid oxide fuel cell (SOFC) development is the reduction of its operating temperature from about 1000 °C to the range of 600–800 °C [1–6], which widens the materials choice for stack components such as the interconnect. Metallic interconnects have gained more and more attention to supplant traditional $LaCrO_3$-based interconnects in recent years [7–10] due to their advantages over the ceramic materials including lower cost, easier processing, better workability, improved mechanical strength, higher electronic conductivity (the ohmic losses in the metallic interconnect can be neglected), higher thermal conductivity (more uniform heat distribution), etc.

Metallic interconnects studied so far include Cr-based [11–13], Fe-based [14–16] and Ni-based [17–19] alloys. In fact, almost all the candidates for metallic interconnects are chromia-forming alloys because of the electrically conductive nature of Cr_2O_3, as compared to Al_2O_3 and SiO_2, which are insulating [20,21]. However, the chromia-forming alloys have an inherent weakness related to the Cr volatization primarily in the form of CrO_3 and $CrO_2(OH)_2$ generated from Cr_2O_3 evaporation in the SOFC operating environments [22]. The volatile Cr species could migrate to and poison the cathode, resulting in significantly reduced cathode activity and subsequent degradation of the SOFC performance [23–26]. Therefore, the formation of a stable, electrically conductive and low Cr-volatility oxide outer layer atop the chromia is highly desirable to reduce or block the vaporization of chromia. Indeed, one commercial alloy Crofer22 APU has been recently developed for SOFC interconnect applications, which upon thermal exposure forms a double-layer oxide structure with $(Mn, Cr)_3O_4$ spinel as the outer layer and Cr_2O_3 as the inner layer [27].

In this paper, a series of Fe–22Cr alloys with compositions similar to Crofer22 APU are investigated. The aims of this study are to determine the effect of alloy purity as well as Mn and Ti contents on the oxidation behavior and the scale area specific resistance (ASR) of the Fe–22Cr alloys, and to compare the performance of these alloys with commercial ferritic alloys such as Crofer22 APU and Ebrite. In addition, a Ni-based alloy Haynes

* Corresponding author. Tel.: +1 931 372 3186; fax: +1 931 372 6340.
E-mail address: jzhu@tntech.edu (J. Zhu).

0378-7753/$ – see front matter © 2006 Elsevier B.V. All rights reserved.
doi:10.1016/j.jpowsour.2006.02.028

Table 1
Chemical compositions of the alloys (wt.%)

	Ni	Fe	Cr	Mo	Mn	Co	Si	Al	Ti	C	S	La
Ebrite		Balanced	26	1	0.01		0.025			0.001	0.02	
Crofer22 APU		Balanced	22		0.45		0.1		0.08	0.005	0.002	0.06
#1		Balanced	22		0.4				0.3	<0.002	<0.001	
#2		Balanced	22		0.7				0.3	<0.002	<0.001	
#3		Balanced	22		0.45				0.06	<0.002	<0.001	0.08
#4		Balanced	22		0.45					<0.002	<0.001	0.08
#5		Balanced	22		0.45				0.06	<0.002	<0.001	
Haynes 242	Balanced	2[a]	8	25	0.8[a]	2.5[a]	0.8[a]	0.5[a]		0.03*		

[a] Maximum.

242 is included in the evaluation, which exhibits a relatively low coefficient of thermal expansion (CTE) and a potential to form an NiO outer layer atop a chromia inner layer upon thermal exposure [28]. The potential of these alloys as intermediate-temperature SOFC interconnects will be discussed based on the experimental results.

2. Experimental

Eight alloys, seven ferritic alloys and one Ni-based alloy, were selected in this study and the compositions are listed in Table 1 (all the compositions given in this paper are in wt.%). Ebrite is a commercial alloy based on Fe–26% Cr steel with about 1% Mo and a trace amount of Mn, while Crofer22 APU is a recently developed interconnect alloy with 22% Cr, 0.45% Mn, 0.08% Ti and 0.06% La. Alloys #1–5, which were made in our laboratory via arc-melting/drop casting followed by hot and cold rolling to 1 mm thick sheets, are similar in composition to Crofer22 APU with different levels of Mn and Ti additions. Ultra-high purity raw materials were used for making Alloys #1–5. As shown in Table 1, the quantitative analysis indicated that the impurities such as carbon and sulfur in Alloys #1–5 were much lower than the commercial alloys. The alloy specimens, of 1 cm × 1 cm × 1–2 mm in size, were ground to 800 grits using SiC sand papers, followed by ultrasonic cleaning in acetone. The cyclic oxidation test was carried out in air in a box furnace where specimens were hung in alumina crucibles. Each cycle consisted of 100 h at 800 °C, followed by air cooling to room temperature. The specimens were cycled to 20 cycles which corresponded to a cumulative oxidation time of 2000 h. The phase structure of the oxide scale was determined by X-ray diffraction (XRD). The scale morphology was observed using scanning electron microscopy with an energy-dispersive X-ray analysis attachment (SEM/EDX).

The ASR of the oxide scales formed on these alloys after the oxidation test was measured from 500 to 800 °C using the two-probe four-point method, as described previously [29]. Two of the oxidized surfaces were covered with Pt paste (the diameter of the covered circular area was 0.78 cm), and two Pt meshes each with two Pt leads were placed on the top of the paste for current collection. After firing of the paste, a constant current was applied across two Pt leads using a current source, and the corresponding voltage across the other two Pt leads was measured using a multimeter. In this experiment, the variation of voltage across the specimens under different currents ranging from 1 to 100 mA was verified to follow Ohm's law exactly, which indicated that the interfacial polarization was negligible within the applied current range. A constant current of 10 mA was used in the measurement. The electrical resistance was calculated according to Ohm's law, $R = V/2I$, where I is the current (10 mA) applied to the specimen through two Pt leads and V is the voltage drop across the sample measured with the other two Pt leads. A factor of 2 was included to account for the fact that the voltage drop was measured across two oxide scales. The ASR was equal to R multiplied by the area covered by the Pt paste.

3. Results

3.1. Oxidation kinetics

Fig. 1 shows the mass changes of all the alloys during cyclic oxidation in air at 800 °C. It is apparent that the mass gain of Alloy #2 was the largest among these alloys, close to that of Alloy #1, and slightly larger than that of Alloy #4. The weight gain of Alloy #5 was almost the same as that of Crofer22 APU, and slightly higher than that of Alloy #3. The mass gain of Ebrite was the smallest among the ferritic alloys used in this study and

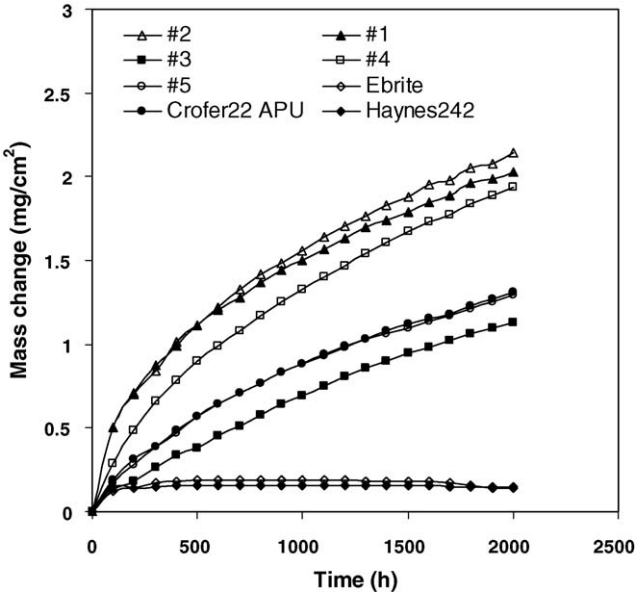

Fig. 1. Oxidation kinetics of the alloys in air at 800 °C for twenty 100-h cycles.

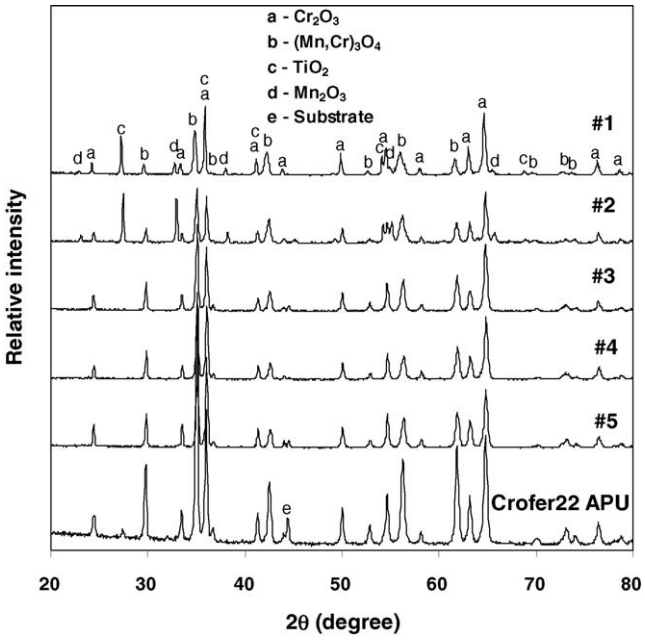

Fig. 2. XRD patterns of the oxidized Fe–22Cr series alloy coupons.

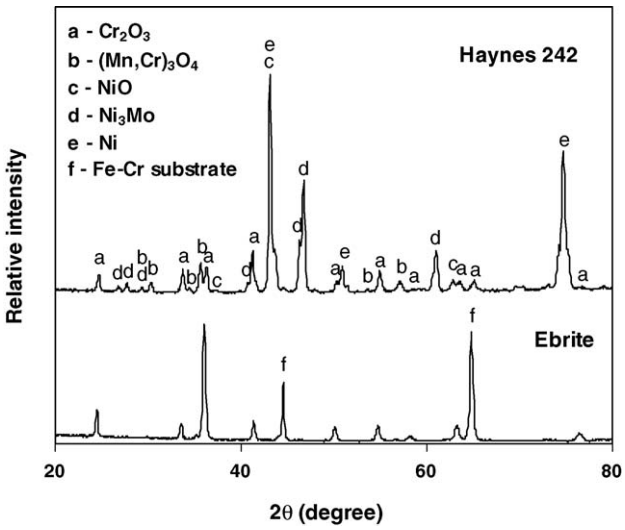

Fig. 3. XRD patterns of the oxidized Ebrite and Haynes 242 coupons.

similar to that of Haynes 242. The weight of Ebrite had a trend to drop after 1500 h because of chromium evaporation from the Cr_2O_3 scale formed on the alloy surface. In comparison, the mass of Haynes 242 was almost constant after the initial stage of oxidation. No oxide scale spallation was observed for any of these alloys after the cyclic oxidation test.

3.2. Phase structure and morphology of the oxide scales

The XRD patterns of the oxide scales formed on the Fe–22Cr series alloys after 20 cycles are presented in Fig. 2. The oxide scales developed on these alloys consisted mainly of Cr_2O_3 and $(Mn, Cr)_3O_4$ except that TiO_2 was formed on Alloys #1 and #2 and Crofer22 APU, and Mn_2O_3 was also detected for Alloys #1 and #2. Fig. 3 indicates that the oxide scale formed on Haynes 242 after 20 cycles was composed of NiO, Cr_2O_3 and $(Mn, Cr)_3O_4$. A relatively pure Cr_2O_3 scale was established on the Ebrite coupon. As shown in Fig. 2, for the Fe–22Cr series alloys, a relatively larger amount of Ti addition led to the formation of TiO_2 on the surface. For example, after cyclic oxidation the surface morphology of the coupon of Alloy #1 containing 0.3% Ti was different from that of Alloy #4 which is free of Ti, as shown in Fig. 4. For Alloy #1, the oxide top layer consisted of TiO_2 and Mn_2O_3, while only $(Mn, Cr)_3O_4$ was detected on the surface of Alloy #4.

In order to verify the oxide phase locations within the oxide scale formed on Alloy #1, one coupon after the 20-cycle exposure was slightly polished step by step, and the XRD patterns were obtained after each step, as shown in Fig. 5. It is clear that for Alloy #1, Mn_2O_3 and TiO_2 were on top of the $(Mn, Cr)_3O_4$ spinel layer beneath which was the Cr_2O_3 inner layer. Cross-sectional views of the oxide scales formed on the different alloys after 20 cycles are shown in Fig. 6. The cross-sectional distribution of the various oxides in the thermally grown scale on Alloy #1 was similar to that on Alloy #2. As shown in Figs. 4–6a and b, the oxide scales formed on Alloys #1 and #2 consisted of a very thin top layer of Mn_2O_3 and TiO_2, a thin sub-layer of $(Mn, Cr)_3O_4$ spinel and a relative thick Cr_2O_3 inner layer in contact with an internal oxidation zone of mainly TiO_2 particles.

The oxide scale formed on Alloy #3 was similar to that on Alloy #5 as shown in Fig. 6c and e: the exterior layer was (Mn,

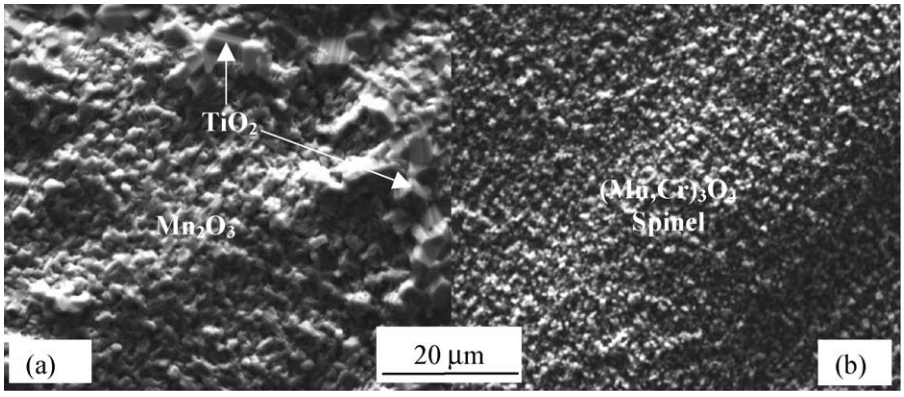

Fig. 4. Surface morphologies of the oxidized coupons: (a) Alloy #1 and (b) Alloy #4.

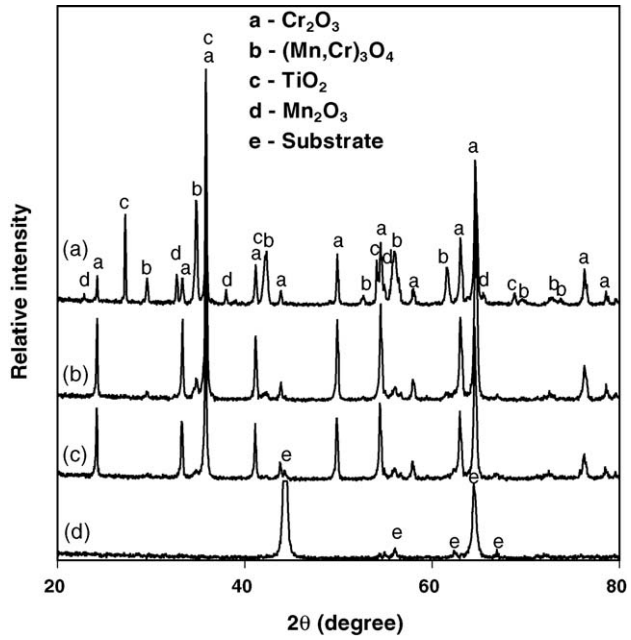

Fig. 5. XRD patterns of the oxidized coupon of Alloy #1: (a) without polishing, (b) after slight surface polishing, (c) after further polishing and (d) after complete removal of the surface oxide scale.

$Cr)_3O_4$ and the inner layer was Cr_2O_3 which was followed by internal oxide particles of TiO_2. The oxide scale formed on Alloy #4, as shown in Fig. 6d had a double-layer structure, close to that formed on Alloys #3 and #5, except that no internal oxidation was observed, as this alloy was free of Ti. In addition, a double-layer oxide structure consisting of a spinel outer layer with a small amount of TiO_2 particles and a Cr_2O_3 inner layer was also formed on Crofer22 APU as shown in Fig. 6f. The oxide scale thermally grown on Haynes 242 was composed of an NiO top layer and a Cr_2O_3 inner layer with certain amount of (Mn, $Cr)_3O_4$; in addition, some Al_2O_3 particles were observed underneath the Cr_2O_3 scale, as shown in Fig. 6g. It should be noted that the thickness of the NiO outer layer was not very uniform. For Ebrite, only a single Cr_2O_3 layer was formed, as shown in Fig. 6h. It is conspicuous that no voids were observed at the interface of the oxide scale and alloy substrate for Alloys #1–5. However, some voids existed between the Cr_2O_3 layer and alloy substrate for Crofer22 APU and Ebrite.

3.3. ASR of the oxide scales

The scale ASR for different alloys is plotted in Fig. 7. For the Fe–22Cr series alloys, the scale ASR for Alloys #1 and #2 was almost the same, while the scale ASR for Alloy #3 was similar to that formed on Crofer22 APU. For the Fe–22Cr series alloys, the effect of Ti content in the alloys on the scale ASR is obvious: the higher the Ti content is in the alloys, the lower the scale ASR. As an example, the scale ASR for Alloys #1 and #2 was lower than that of the scale for Alloy #3 and Crofer22 APU, although the oxide scale formed on Alloys #1 and #2 was thicker than that on Alloy #3 and Crofer22 APU, as shown in Fig. 6. The Ti content in Alloy #3 was the same as that in Alloy #5, but the scale ASR for Alloy #3 was lower than that for Alloy #5 because the oxide scale formed on Alloy #3 was thinner than that on Alloy #5. The scale ASR for Alloy #4 which was free of Ti was the highest among the Fe–22Cr series alloys.

The effect of Mn content on the scale ASR for the Fe–22Cr alloys was not noticeable. The scale ASR for Alloy #1 with 0.4% Mn was very close to that for Alloy #2 with 0.7% Mn. The scale ASR for Ebrite was similar to that of Crofer22 APU, although it had a thinner oxide scale than Crofer22 APU. The scale ASR for Haynes 242 was the lowest among all the investigated alloys.

4. Discussion

4.1. Oxidation resistance

The effect of Mn and Ti contents on the oxidation kinetics of the ferritic alloys is significant. The higher the contents of Mn and Ti are in the alloys, the larger the weight gain. This is most likely due to the high diffusivity of Ti and Mn ions in chromia which accelerates the oxidation rate of these alloys [30,31]. As shown in Fig. 1 and Table 1, the mass gain of Alloy #2 was the largest among these alloys and slightly higher than that of Alloy #1. However, the mass gain of Alloy #4 without Ti was higher than that of Alloy #3 containing minor Ti (0.06%). The reason is not clear, and might be due to the complex interaction between Mn, Ti and La. The mass gain of Ebrite was the lowest among the ferritic alloys because it contained a highest amount of Cr, only a trace amount of Mn, and was free of Ti.

Minor La addition improved the oxidation resistance of the ferritic alloys via the so-called reactive element effect [32]. For example, the mass gain of Alloy #3 with 0.08% La was slightly lower than that of Alloy #5 without La. In addition, the composition of Alloy #3 was almost the same as that of Crofer22 APU, but the oxidation rate of Alloy #3 was slightly lower than that of Crofer22 APU. This might result from the high alloy purity of Alloy #3. As shown in Table 1, the impurities such as carbon whose content in Alloy #3 was less than that in Crofer22 APU, could have a detrimental effect on the oxidation resistance [33]. Furthermore, compared to Ebrite and Crofer22 APU, the interface between the oxide scale and alloy substrate for Alloys #1–5 was free of voids, which again is likely related to the high alloy purity.

Although the Cr content in Haynes 242 was lower than that in Ebrite, these two alloys exhibited similar oxidation kinetics. This might result from the fact that a dense Cr_2O_3 scale was formed on both of them. The formation of an NiO top layer will increase the oxidation rate of Haynes 242, while the lower diffusion coefficient of Cr in the Ni–Cr system than in the Fe–Cr system [34] is expected to have an opposite effect on the oxidation rate of Haynes 242.

4.2. Oxide structure and oxidation mechanism

From Figs. 2 and 4–6, the oxide outer layer in the scale formed on Alloys #1 and #2 consisted of a mixed TiO_2/Mn_2O_3 top layer and a (Mn, $Cr)_3O_4$ sub-layer, while the outer layer formed on

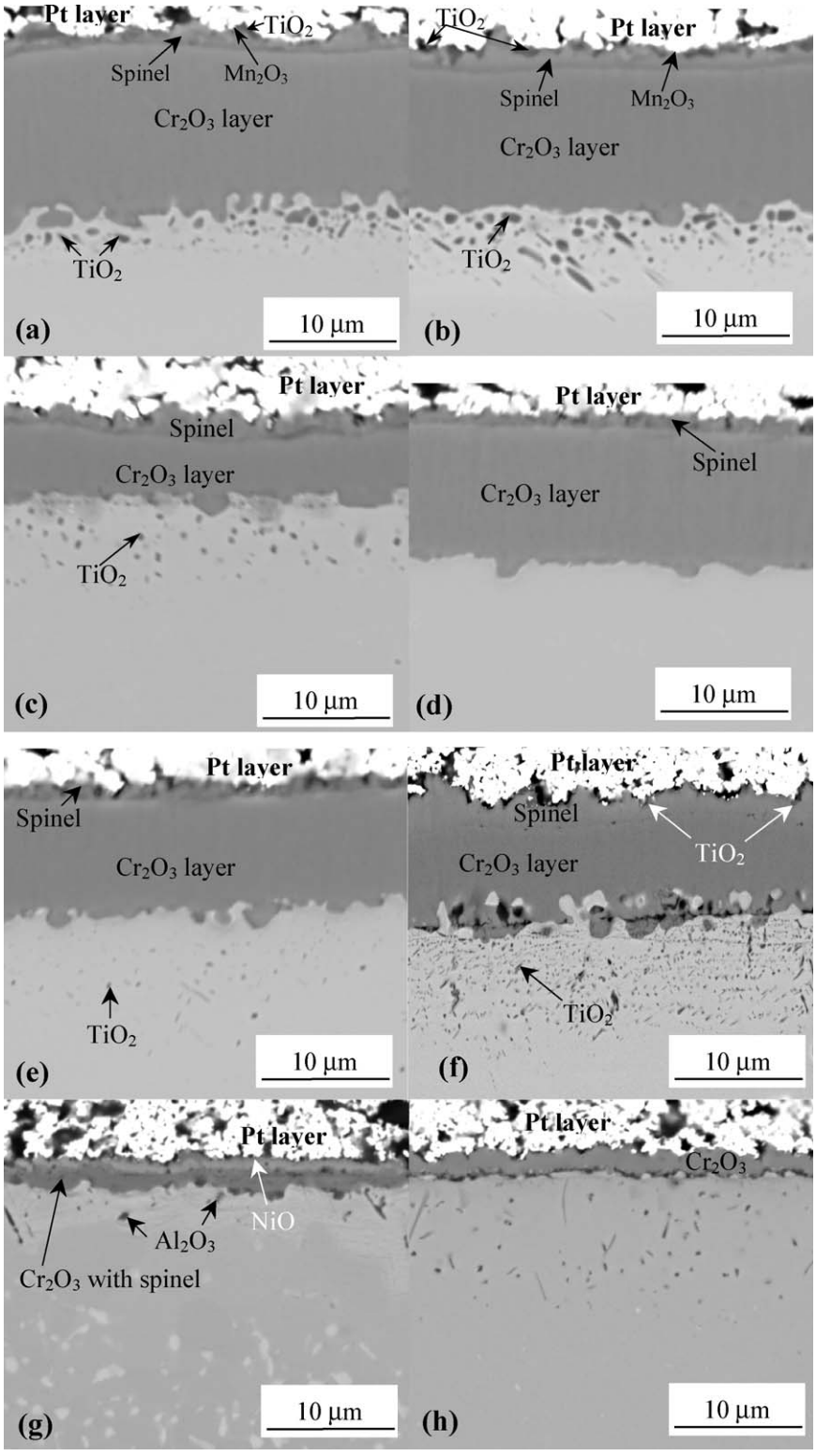

Fig. 6. Cross-sections of the oxidized alloy coupons: (a) Alloy #1, (b) Alloy #2, (c) Alloy #3, (d) Alloy #4, (e) Alloy #5, (f) Crofer22 APU, (g) Haynes 242 and (h) Ebrite.

Alloys #3–5, and Crofer22 APU was mainly comprised of $(Mn, Cr)_3O_4$. The XRD patterns in Fig. 5 and the surface morphology in Fig. 4a indicate that TiO_2 was formed in the outermost layer in the oxide scale because of high mobility of Ti ions in Cr_2O_3 [30]. Initially, the Cr_2O_3 layer growth is governed by outward solid-state diffusion of the Cr cationic vacancies. Ti induces the creation of additional cationic vacancies in the Cr_2O_3 layer when Ti ion replaces Cr ion [35,36]. The cationic vacancy increase in the Cr_2O_3 layer will induce faster Cr diffusion and subsequently a higher oxidation rate [37].

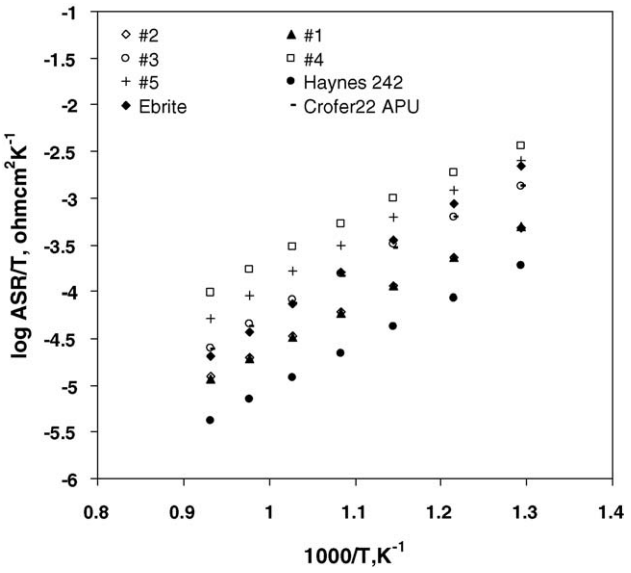

Fig. 7. The scale ASR of the oxidized alloy coupons.

The reduced oxidation resistance of the alloys containing Ti and Mn could also be partially attributed to the influence of Mn in the alloys. Mn ion diffuses faster than Cr^{3+} via Cr^{3+}-lattice sites in Cr_2O_3 [31], which leads to the enrichment of Mn at the oxide scale/air interface and the subsequent formation of an (Mn, Cr)$_3O_4$ spinel layer over the Cr_2O_3 layer. From Figs. 5 and 6a and b, it is obvious that a thin layer of mixed Mn_2O_3 and TiO_2 was formed atop the (Mn, Cr)$_3O_4$ spinel layer for Alloys #1 and #2. Most likely, a higher Ti content further promoted the outward diffusion of Mn ions in Cr_2O_3 [31], leading to the co-precipitation of Mn_2O_3 with TiO_2 over the (Mn, Cr)$_3O_4$ spinel layer [38]. Since this top layer is Cr-free, it is potentially beneficial in further mitigating the Cr evaporation from the interconnect alloy.

During high temperature oxidation, outward diffusion of metal cations such as Cr, Ti and Mn ions is simultaneously accompanied by inward diffusion of oxygen anions across a thermally grown oxide scale. Since metals or alloys typically have an appreciable solubility for oxygen [39], oxygen can dissolve into the alloy substrate near the oxide scale through diffusion along the fast diffusion paths such as grain boundaries, and react with the alloying elements that have higher oxygen affinity to form an internal oxidation zone. As Ti has the highest affinity with oxygen among all the alloying elements in the Fe–22Cr series alloys, TiO_2 particles were formed underneath the Cr_2O_3 scale as the internal oxidation products indicated in Fig. 6a–c and e, which also contributed to the mass gain of the Fe–22Cr alloys containing Ti.

The oxide scale grown on Haynes 242 consisted of an NiO outer layer and a Cr_2O_3 inner layer with some (Mn, Cr)$_3O_4$ spinel, as indicated in Figs. 3 and 6g. During the beginning stage of oxidation, Ni rather than Cr was oxidized due to a low Cr content in the alloy, leading to the formation of an NiO outer layer. Upon the establishment of the NiO layer, the oxygen partial pressure at the interface between the NiO and alloy substrate became sufficiently low to promote the selective oxidation of Cr, resulting in the formation of the Cr_2O_3 inner layer. Simultaneously, a small amount of (Mn, Cr)$_3O_4$ spinel was produced due to the rapid diffusion of Mn ions in the Cr_2O_3 layer. As shown in Fig. 1, the oxidation for Haynes 242 was faster than that for Ebrite during the beginning stage of oxidation as a result of the NiO formation.

Table 2
Physical properties of some oxides

Oxide	CTE (25–1000 °C) × 10^{-6} (°C^{-1})	Electrical resistivity (Ω cm)
Cr_2O_3	9.6	100 at 800 °C
$Mn_{1.5}Cr_{1.5}O_4$	7.5	20 at 800 °C
NiO	14	5–7 at 900 °C
TiO_2	7–8	100 at 900 °C
Mn_2O_3	–	0.7–1 at 800 °C

4.3. Electrical properties of the oxide scales

For the ferritic alloys, although the oxidation resistance of the Fe–22Cr series alloys including Crofer22 APU was inferior to that of Ebrite, the ASR of the oxide scales formed on some of them was comparable to that of Ebrite. As shown in Fig. 7, the scale ASR for Alloys #1 and #2 was lower than that for Ebrite, and the scale ASR for Alloy #3 and Crofer22 APU was similar to that for Ebrite. The scale ASR for Alloy #3 was lower than that for Alloy #5, which is due to the fact that the oxide scale formed on Alloy #5 was thicker than that on Alloy #3 which had a small amount of La addition to improve its oxidation resistance.

The oxide scales formed on Alloys #1 and #2 were the thickest amongst these alloys; their scale ASR, however, was lower than that of the remaining ferritic alloys. As discussed above, Ti addition in the ferritic alloys not only accelerated the oxidation of these alloys due to fast diffusion of Ti cations across the Cr_2O_3 layer but also promoted outward diffusion of Mn ions in the Cr_2O_3 layer, resulting in the formation of a mixed Mn_2O_3/TiO_2 surface layer and/or a (Mn, Cr)$_3O_4$ spinel layer over the Cr_2O_3 layer. The composition of the spinel layer formed on the Fe–Cr–Mn alloys was found to be close to $Mn_{1.5}Cr_{1.5}O_4$ [40]. Table 2 lists some physical properties for the various oxides [41–45] that might exist in the oxide scales formed on the alloys studied in this paper. As shown in Table 2, the electrical resistance of the mixed Mn_2O_3/TiO_2 and/or spinel layer can be ignored compared to the Cr_2O_3 inner layer, as both Mn_2O_3 and $Mn_{1.5}Cr_{1.5}O_4$ possess significantly higher electrical conductivity than Cr_2O_3, while TiO_2 has a slightly higher electrical resistance than Cr_2O_3; furthermore, the outer layer is much thinner than the Cr_2O_3 inner layer, as shown in Fig. 6.

The lower scale ASR values for Alloys #1 and #2 can be attributed to: (1) a lower electrical resistance of the Cr_2O_3 scale formed on these two alloys than that on the other ferritic alloys and (2) a lower contact resistance between the Pt current collector and Mn_2O_3/TiO_2 than that between Pt/(Mn, Cr)$_3O_4$ and Pt/Cr_2O_3. The Cr_2O_3 scale formed on these two alloys was doped with a saturated amount of TiO_2 as the Ti ions diffused outward across the Cr_2O_3 layer [46,47] and the TiO_2-doped

Cr_2O_3 had a higher electrical conductivity than pure Cr_2O_3 [48]. Therefore, even though Ti addition increased the oxidation rate of the Fe–22Cr series alloys, it improved the electrical conductivity of the oxide scales formed on these two alloys. Overall, the higher the Ti content is in the alloys, the lower the scale ASR: the scale ASR for Alloys #1 and #2 with 0.3%Ti was lower than that for Alloy #3 containing 0.06% Ti and Crofer22 APU with 0.08% Ti; the scale ASR for Alloy #4 free of Ti was the highest among these alloys. Furthermore, the formation of a mixed Mn_2O_3/TiO_2 surface layer was beneficial in lowering the scale ASR because of the extremely low electrical resistivity of Mn_2O_3 in the mixed oxide layer (as listed in Table 2) and possibly lower contact resistance between Pt and Mn_2O_3. While the TiO_2 particles formed on the surface of Alloys #1 and #2 were discontinuous, the TiO_2 particles could become interconnected and form a continuous layer with further outward diffusion of Ti ions after longer term oxidation. If that were the case, a continuous TiO_2 layer might increase the scale ASR due to its slightly higher electrical resistivity than Cr_2O_3, as shown in Table 2.

Although the oxide scale formed on Ebrite was thinner than that on Crofer22 APU, the scale ASR for Ebrite was close to that for Crofer22 APU. The lower scale ASR for Crofer22 APU could be explained by: (1) the formation of the electrically conductive $(Mn, Cr)_3O_4$ spinel outer layer and subsequently reduced contact resistance between Pt and $(Mn, Cr)_3O_4$ and (2) the increase in electrical conductivity of Cr_2O_3 due to TiO_2 doping. In addition, a significant amount of voids existed between the oxide scale and Ebrite substrate, which might increase the resistance to electrical conduction for this alloy. As listed in Table 1, the sulfur content in Ebrite was higher than that in the Fe–22Cr series alloys. These voids might have resulted from the sulfur in the alloys that tends to segregate to the oxide scale/substrate interface, hence deteriorating the scale adherence [49].

From Fig. 7, the scale ASR for Haynes 242 was the lowest among all the alloys. Even though the thickness of the oxide scale formed on Haynes 242 was similar to that on Ebrite (Fig. 6g and h), the oxide outer layer for Haynes 242 was NiO, which possesses an electrical resistivity almost two orders of magnitude lower than that of Cr_2O_3 [45] (see Table 2). Therefore, the electrical resistance of NiO may be ignored compared to Cr_2O_3 and the contact resistance between the Pt and the oxide scale may be reduced due to the presence of the NiO layer, leading to the lower scale ASR for Haynes 242.

4.4. Concern about thermal expansion mismatch

Even though the TiO_2/Mn_2O_3 and/or $(Mn, Cr)_3O_4$ layers formed over the Cr_2O_3 inner layer could reduce the Cr evaporation from the ferritic alloys, one concern with these oxides is their thermal expansion behavior. As shown in Table 2, while the CTE for Mn_2O_3 is currently not available, the CTEs of TiO_2 and $Mn_{1.5}Cr_{1.5}O_4$ are 7–8 $\times 10^{-6}\,^{\circ}C^{-1}$ [43] and 7.5 $\times 10^{-6}\,^{\circ}C^{-1}$ [42], respectively, which are noticeably lower than that of Cr_2O_3 (9.6 $\times 10^{-6}\,^{\circ}C^{-1}$) [43] and ferritic steels (9–12 $\times 10^{-6}\,^{\circ}C^{-1}$) [50]. Such CTE mismatch might contribute to their eventual spallation after longer term cyclic oxidation, therefore losing their function in blocking the chromium from evaporation.

While Haynes 242 exhibited a better performance than the ferritic alloys with regard to the oxidation resistance and scale ASR, the CTE of NiO is 14 $\times 10^{-6}\,^{\circ}C^{-1}$, which is much higher than that of Cr_2O_3 (9.6 $\times 10^{-6}\,^{\circ}C^{-1}$) (as shown in Table 2) and is close to that of Haynes 242 (12–14 $\times 10^{-6}\,^{\circ}C^{-1}$) [28]. The NiO and Cr_2O_3 layers might spall off after long-term cyclic oxidation, due to the large CTE mismatch between the NiO and Cr_2O_3. Indeed, some localized detachment of the NiO layer from the Cr_2O_3 scale was occasionally observed on the cross-section of the cyclically oxidized Haynes 242 coupon.

In summary, both Haynes 242 and the Fe–22Cr series alloys including Crofer22 APU are promising interconnect alloys for intermediate-temperature SOFC, as the mixed Mn_2O_3/TiO_2, $(Mn, Cr)_3O_4$, or NiO outer layer is electrically conductive and could suppress the Cr evaporation from the Cr_2O_3 inner layer. While these oxide layers exhibited an overall good adherence with the Cr_2O_3 layer after 2000 h (20 cycles) in air at 800 °C, longer term cyclic oxidation tests should be conducted to further assess the scale spallation resistance, as their CTE mismatch with Cr_2O_3 might lead to their eventual cracking/spallation during the long-term operation lifetime expected for the SOFC stacks.

5. Conclusions

Based on the cyclic oxidation test results for a number of alloys, the following conclusions can be drawn:

(1) For the Fe–22Cr series alloys containing Mn and/or Ti, a layered oxide scale structure with an $(Mn, Cr)_3O_4$ spinel layer atop a Cr_2O_3 inner layer can be thermally grown on the substrate alloys after the oxidation test. A higher Ti content (0.3 wt.%) promoted the formation of a mixed Mn_2O_3/TiO_2 top layer which was free of Cr, and therefore could potentially further reduce the Cr evaporation rate from the ferritic alloys.
(2) Although the oxidation resistance of the Fe–22Cr series alloys was reduced due to the Ti and Mn additions, their scale ASR was comparable to or even lower than that for Ebrite. The scale ASR could be correlated to the Ti content in these alloys.
(3) High alloy purity slightly improved the oxidation resistance of the ferritic alloys, and drastically reduced the voids at the interface between the Cr_2O_3 scale and alloy substrate.
(4) A double-layer oxide structure with an NiO outer layer and a Cr_2O_3 inner layer was developed on Haynes 242 after cyclic oxidation. The NiO outer layer was Cr-free, and therefore could mitigate the Cr evaporation from the Cr_2O_3 inner layer. Moreover, Haynes 242 possessed superior oxidation resistance and the lowest scale ASR among all the investigated alloys.
(5) Longer term cyclic oxidation tests are needed to further assess the scale spallation resistance of these alloys, as the mismatch in CTE between the different oxide layers in the scale (as well as with the alloy substrate) might cause eventual cracking and spallation of the Cr-blocking outer layer.

Acknowledgements

This study was sponsored by NSF (Grant #DMR-0238113). Additional support was provided by the Center for Manufacturing Research, Tennessee Technological University.

References

[1] S. de Souza, S.J. Visco, L.C. De Jonghe, Solid State Ionics 98 (1997) 57.
[2] S. de Souza, S.J. Visco, L.C. De Jonghe, J. Electochem. Soc. 144 (1997) L35.
[3] H. Ishihara, H. Matsuda, Y. Takita, J. Am. Chem. Soc. 116 (1994) 3801.
[4] M. Feng, J.B. Goodenough, Eur. J. Solid State Inorg. Chem. T31 (1994) 663.
[5] P. Huang, A. Petric, J. Electrochem. Soc. 143 (5) (1996) 1644.
[6] K.Q. Huang, R. Tichy, J.B. Goodenough, J. Am. Ceram. Soc. 81 (1998) 2565.
[7] T. Horita, Y.P. Xiong, K. Yamaji, N. Sakai, H. Yokokawa, J. Power Sources 118 (2003) 35.
[8] Z. Zeng, K. Natesan, Solid State Ionics 167 (2004) 9.
[9] K. Huang, P.Y. Hou, J.B. Goodenough, Solid State Ionics 129 (2000) 237.
[10] J.W. Fergus, Mater. Sci. Eng. A397 (2005) 271.
[11] S. Linderoth, P.V. Hendriksen, M. Mogensen, N. Langvad, J. Mater. Sci. 31 (1996) 5077.
[12] U.v.d. Crone, M. Hansel, W.J. Quadakkers, R. Vaβen, Fresenius J. Anal. Chem. 358 (1997) 230.
[13] W.J. Quadakkers, M. Hänsel, T. Rieck, Mater. Corros. 49 (1998) 252.
[14] T. Brylewski, M. Nanko, T. Maruyama, K. Przybylski, Solid State Ionics 143 (2) (2001) 131.
[15] W.J. Quadakkers, J. Piron-Abellan, V. Shemet, L. Singheiser, Mater. High Temp. 20 (2) (2003) 115.
[16] H. Kurokawa, K. Kawamura, T. Maruyama, Solid State Ionics 168 (1–2) (2004) 13.
[17] J. Li, J. Pu, J.Z. Xiao, X.L. Qian, J. Power Sources 139 (2005) 182.
[18] D.M. England, A.V. Virkar, J. Electrochem. Soc. 148 (4) (2001) A330.
[19] Y. Yamazaki, T. Namikawa, H. Michihata, J. Chem. Soc. Jpn. 8 (1988) 1329.
[20] P. Kofstad, R. Bredesen, Solid State Ionics 52 (1992) 69.
[21] Z.G. Yang, K.S. Weil, D.M. Paxton, J.W. Stevenson, J. Electrochem. Soc. 150 (9) (2003) A1188.
[22] K. Hilpert, D. Das, M. Miller, D.H. Peck, R. Weiβ, J. Electrochem. Soc. 143 (11) (1996) 3642.
[23] S.P. Simner, M.D. Anderson, G.G. Xia, Z.G. Yang, L.R. Pederson, J.W. Stevenson, J. Electrochem. Soc. 152 (4) (2005) A740.
[24] Y. Matsuzaki, I. Yasuda, Solid State Ionics 132 (2000) 271.
[25] Y.S. Taniguchi, M. Kadowaki, H. Kawamura, T. Yasuo, Y. Akiyama, Y. Miyake, J. Power Sources 55 (1995) 73.
[26] Y. Matsuzaki, I. Yasuda, J. Electrochem. Soc. 148 (2001) A126.
[27] Z.G. Yang, J.S. Hardy, M.S. Walker, G. Xia, S.P. Simner, J.W. Stevenson, J. Electrochem. Soc. 151 (11) (2004) A1825.
[28] S.J. Geng, J.H. Zhu, Z.G. Lu, Solid State Ionics 177 (2006) 559.
[29] J.H. Zhu, Y. Zhang, A. Basu, Z.G. Lu, M. Paranthaman, D.F. Lee, E.A. Payzant, Surf. Coat. Technol. 177–178 (2004) 65.
[30] F. Abe, H. Araki, H. Yoshida, M. Okaka, Oxid. Met. 27 (1987) 21.
[31] M.G.E. Cox, B. McEnanay, V.D. Scott, Philos. Magn. 26 (1972) 839.
[32] P.Y. Hou, J. Stringer, Mater. Sci. Eng. A202 (1995) 1.
[33] D. Naumenko, J. Le-Coze, E. Wessel, W. Fischer, W.J. Quadakkers, Mater. Trans. 43 (2002) 168.
[34] B. Cbattopadbyay, G.C. Wood, Oxid. Met. 2 (1970) 373.
[35] A. Holt, P. Kofstad, Solid State Ionics 117 (1999) 21.
[36] J.J. Partyka, J. Eur. Ceram. Soc. 17 (1997) 1597.
[37] C. Issartel, H. Buscail, E. Caudron, R. Cueff, F. Riffard, S. EI Messki, N. Karimi, L. Antoni, Mater. Sci. Forum 461–464 (2004) 69.
[38] D.L. Douglass, F. Gesmundo, C. de Asmundis, Oxid. Met. 25 (1986) 235.
[39] P. Kofstad, High-Temperature Corrosion, Elsevier, Amsterdam, 1988.
[40] T. Brylewski, J. Dabek, K. Przybylski, J. Therm. Anal. Calorim. 77 (2004) 207.
[41] Z.G. Lu, J.H. Zhu, E.A. Payzant, M.P. Paranthaman, J. Am. Ceram. Soc. 88 (4) (2005) 1050.
[42] J.H. Zhu, Z.G. Lu, S.J. Geng, W.D. Porter, Unpublished Results, Tennessee Technological University, 2005.
[43] W.Z. Zhu, S.C. Deevi, Mater. Sci. Eng. A348 (2003) 227.
[44] J. Pattanayak, V. Sitakara Rao, H.S. Maiti, J. Mater. Sci. Lett. 8 (1989) 1405.
[45] H. Ling, A. Petric, Electrochemical Society Proceedings, vol. 2005-07, 1866.
[46] H.B. Grübmeier, A. Naoumidis, H.A. Schulze, J. Vac. Sci. Technol. A4 (1986) 2565.
[47] S. Kamiya, S. Hiramo, S. Somiya, J. Solid State Chem. 28 (1979) 21.
[48] H. Nagai, K. Ohbayahi, J. Am. Ceram. Soc. 72 (1989) 400.
[49] H.J. Grabke, D. Wiemer, H. Viefhaus, Appl. Surf. Sci. 47 (1991) 243.
[50] N.Q. Minh, T. Takahashi, Science and Technology of Ceramic Fuel Cells, Elsevier, Amsterdam, 1995.